Accuracy of Superlocalization Imaging Using Gaussian and Dipole Emission Point-Spread Functions for Modeling Gold Nanorod Luminescence

Eric J. Titus and Katherine A. Willets*

Department of Chemistry, The University of Texas at Austin, 105 East 24th Street STOP A5300, Austin, Texas 78712, United States

ABSTRACT We present a study comparing the accuracy of superlocalization imaging of plasmon-mediated emission from gold nanorods (AuNRs) using both Gaussian and dipole emission point-spread function (PSF) models. By fitting the emission PSF of single AuNR luminescence, we have shown that a 3-axis dipole PSF gives improved localization accuracy over the Gaussian PSF, especially for nonplanar AuNRs, while also allowing the AuNR three-dimensional orientation and emission wavelength to be determined. On the other hand, when a single-axis dipole PSF model is applied to the AuNR emission, the fit estimates converge to values that are inconsistent with their experimentally measured values, affecting both the localization accuracy and precision of the fitted centroid position. These results indicate that when applying superlocalization techniques to plasmonic nanostructures, care must be taken to understand the nature of the emission before a correct dipole PSF can be applied.

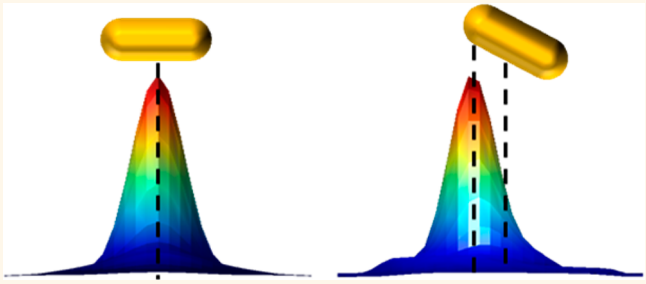

KEYWORDS: super-resolution imaging · point spread function · gold nanorod · luminescence · centroid

Noble metal nanoparticles (~100 nm particles of silver and gold) have proven useful in areas such as biosensing,[1,2] photothermal therapy,[3,4] and surface enhanced spectroscopies[5,6] due to their unique optical properties, including intense light scattering and strongly enhanced near-field radiation at their surfaces upon excitation with visible light.[7] These optical properties are due to resonant, light-driven collective oscillations of the surface conduction electrons within the nanoparticles, which are known as localized surface plasmons. One challenge when studying the optical properties of plasmonic nanostructures is the small size of the particles relative to the wavelength of light, which places them well below the optical diffraction limit. To overcome the diffraction limit, super-resolution imaging techniques have been applied to plasmonic nanostructures to track nanoparticle motion,[8−12] study ligand binding,[13,14] follow catalytic processes in real time,[15] and map plasmonically excited electromagnetic "hot spots."[16−21]

In super-resolution microscopy, emission from a single, diffraction-limited spot is imaged onto a 2-dimensional (2-D) detector, and the center of the emission, or centroid, is extracted by fitting the point spread function (PSF) of the emission to some model function.[22−24] The PSF is often approximated as a 2-D Gaussian in these studies, due to the robustness and low computational expense of this model. While super-resolution imaging regularly yields sub-5 nm resolution and has successfully reproduced structural features of the plasmonic nanostructures under study,[13,15] the accuracy of the centroid localization depends on how well the experimental emission PSF is modeled as a 2-D Gaussian.[14,25−28]

In single molecule fluorescence, nonuniform emission from a single dipole at an interface causes anisotropy in the PSF, which is not captured by the 2-D Gaussian model[29−32] Early single molecule fluorescence studies recognized that this anisotropy could be exploited to determine the 3-dimensional orientation of the emitter,

* Address correspondence to kwillets@cm.utexas.edu.

Received for review May 6, 2013 and accepted June 2, 2013.

Published online June 02, 2013
10.1021/nn4022845

especially upon slight defocusing of the image.[29−34] By modeling the dipolar emission PSF—accounting for the orientation of the emitter, the effects of any refractive index interfaces, and the imaging optics—excellent agreement between experimentally measured PSFs and the calculated patterns were obtained.[29,30,33,34] Later work from Enderlein and Selvin showed that the centroid position determined using this more rigorous dipolar PSF model could differ from the centroid position from a 2-D Gaussian fit by more than 10 nm, depending on photon counts, numerical aperture and detector pixel size, suggesting that the dipolar PSF model would provide superior localization accuracy when fitting experimental PSF data.[25] Subsequent single-molecule super-resolution studies have further substantiated that 2-D Gaussian models can introduce significant errors in the localization accuracy of the centroid, especially for dipoles that are tilted out-of-plane relative to the sample surface.[26−28] Thus, several researchers have suggested that the dipole PSF model should be used in place of a 2-D Gaussian for fitting single-molecule fluorescence data to provide more accurate and rigorous centroid localization for super-resolution imaging.[25−27]

While the dipole-emission PSF has been successfully applied to single-molecule fluorescence, an accurate description of the emission PSF from systems involving nanoparticles can be more complicated. In the case of nanoparticle luminescence (such as the case of gold nanorods) or surface-enhanced Raman scattering (SERS), the emission is coupled out through the plasmon modes of the nanostructure.[35−43] Because dipolar plasmons are usually the strongest contributors to emission in these cases, we expect that a dipolar emission PSF could serve as an appropriate model of the experimental PSF.[38,39,41−44] However, unlike single fluorophores, which behave as single dipoles, plasmonic nanoparticles often support multiple dipole modes and may have contributions from nonplasmonic emission which can complicate the PSF.[17−19,35−37,40,45] Thus, it is important to consider different PSF models to determine which provides the best fit to the experimental data, and therefore the optimal centroid localization accuracy.

In the following study, we compare different PSF models for fitting the luminescence emission from isolated gold nanorods (AuNRs) in order to determine how each model affects the localization accuracy of the calculated centroid. We compare the results of fits using a single-dipole PSF, a multidipole (3-axis) PSF, and a 2-D Gaussian model. We chose AuNRs for this study because they have a strong luminescence signature that is dominated by the longitudinal plasmon mode, suggesting that a dipole PSF is an appropriate model.[35,37] Moreover, both the scattering and luminescence from this system have been previously described using single- and multidipole PSF models to determine the 3-dimensional orientation of single AuNRs.[35,37,44−48] In those studies, images were either defocused by hundreds of nanometers (or more) or the sample surface was modified to highlight the asymmetry inherent to the PSF. However, for centroid localization, we choose to work close to the microscope focus and use a standard coverslip to preserve a high signal-to-noise ratio and work closer to realistic super-resolution imaging conditions. Here, we not only obtain 3-dimensional orientation information, which we compare to the AuNR structure as determined by atomic force microscopy (AFM), but we also obtain the centroid position associated with each fit, which allows us to understand how different plasmon modes contribute to the overall PSF of AuNR emission.

RESULTS AND DISCUSSION

For each diffraction-limited spot associated with single AuNR luminescence, three different models were used to fit the data. The first model is based upon a 2-D Gaussian, as given by eq 1:

$$I(x, y) = z_0 + I_0 e^{\{-[1/2][((x - x_0)/s_x)^2 + ((y - y_0)/s_y)^2]\}} \quad (1)$$

In this expression, $I(x,y)$ represents the intensity of the diffraction-limited spot as a function of position, z_0 is the intensity of the background, I_0 is the peak intensity of the diffraction-limited spot, s_x and s_y are the widths of the Gaussian, and x_0 and y_0 represent the centroid position. This model has been the dominant fitting approach in previous super-resolution imaging studies exploring plasmon-mediated emission processes and will serve as a reference for the other fitting models.[13−20]

For the dipolar PSF models (both single- and multidipole), we modified code made available online by Jörg Enderlein.[49] This model calculates the PSF of a multidipole emitter at an interface, allowing for different contributions from three orthogonal dipolar axes, while taking into account refraction at the interface, how the PSF is distorted by the imaging system, and pixilation of the PSF by the detector.[33,50,51] When fitting experimental AuNR luminescence data with this dipole PSF, static microscope parameters were held constant; these fixed parameters were the numerical aperture of the objective; the magnification of the microscope (measured using a USAF-1951 resolution test target and confirmed *via* AFM, see Supporting Information Section 3); the refractive indices of the glass coverslip, microscope immersion oil, and imaging medium; and the distance of the AuNR from the surface. The parameters that were fit were the defocus of the microscope, the wavelength of emission (λ), the azimuthal and inclination angles of the longitudinal dipole mode (φ and θ, as defined in Figure 1A), intensity, background, centroid position, and the contribution of each dipole component to the total emission intensity

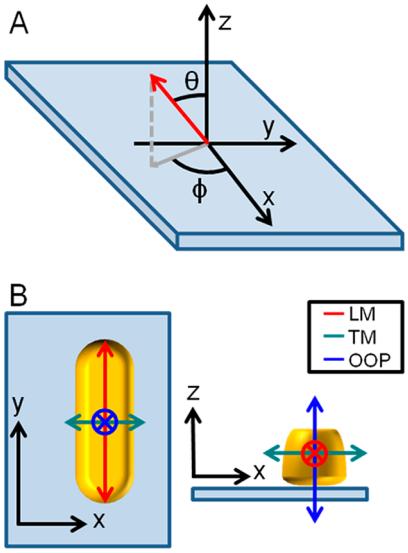

Figure 1. Diagram of coordinate axes relative to the sample plane ($x-y$) and optical axis of the microscope (z). (A) The dipole orientation angles φ and θ correspond to the orientation of the LM dipole mode shown in red on the AuNR in (B). (B) Definitions of the LM, TM, and OOP dipole modes relative to the coordinate axes for a nanorod with $\varphi = 90°/270°$ and $\theta = 90°$ (the in-plane nature of the dipole makes the φ value symmetric along the y-axis).

defined through parameters κ and R as shown in eq 2.

$$I_{total} = RI_{LM} + (1-R)\left(\frac{1+\kappa}{2} I_{TM} + \frac{1-\kappa}{2} I_{OOP}\right) \quad (2)$$

In this expression, I_{LM}, I_{TM} and I_{OOP} represent the vector emission from each orthogonal dipole component as shown in Figure 1B, where the longitudinal mode (LM) is defined along the longitudinal dipole axis of the AuNR, the transverse mode (TM) along the transverse axis parallel to the substrate, and the out-of-plane (OOP) axis defined perpendicular to the substrate. Because the three dipole components are fixed relative to each other, rotating the longitudinal mode by φ and θ will result in a corresponding rotation of the transverse and out-of-plane dipole modes as well.

Based on previous studies, AuNR luminescence is strongly coupled to the longitudinal plasmon mode of the AuNR;[35,37,52,53] this should cause the majority of emission to be polarized along the long axis of the AuNR, allowing for the possibility of fitting this emission to a single-axis dipole PSF. To explore this, we set $R = 1$ in eq 2 and fit our data to a PSF associated with a single emitting dipole; this single-axis dipole fit is referred to as a 1-dipole fit in the remainder of the manuscript. On the other hand, although the majority of emission should be *via* the longitudinal plasmon mode of the AuNR, a small, depolarized amount of emission centered around the transverse plasmon peak has been observed in AuNR luminescence spectra as well, indicating the possible need to model the emission PSF of AuNR luminescence using a 3-axis dipole.[35,37] Previous work using defocused PSF images

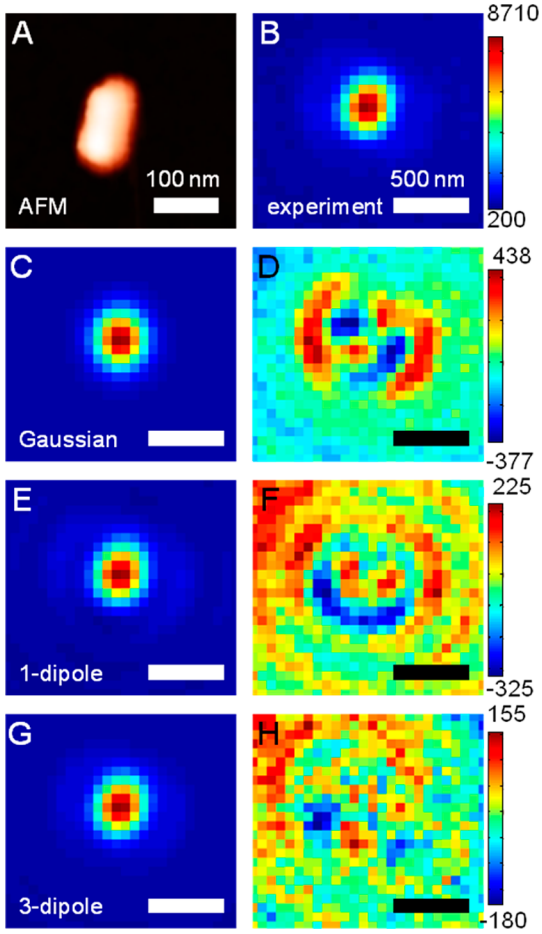

Figure 2. Comparison of different fits and corresponding residuals for AuNR 1. (A) AFM image of AuNR 1, with ~40 nm maximum height. (B) Experimental AuNR 1 luminescence image. (C) Fit and (D) residuals of AuNR luminescence data using the 2-D Gaussian model. (E) Fit and (F) residuals using the 1-dipole PSF model. (G) Fit and (H) residuals using the 3-dipole PSF model with a single emission wavelength. Images B–H share a common 500 nm scale bar.

to probe AuNR orientation have shown that this 3-axis dipole model provides better overall fits to the data.[45,47] In this case, both R and κ are allowed to vary in our fits, in order to determine the relative contributions of each dipole mode (LM, TM, OOP) to the overall intensity. This fit is referred to as a 3-dipole fit for the remainder of the manuscript. For the bulk of our studies, the 3-dipole fit will be performed by fitting emission from all three dipole modes to a single wavelength value (3-dipole, single λ), although we will also test fits in which we allow each individual dipole component to emit at its own distinct wavelength (3-dipole, multi λ).

To compare the accuracy of the different PSF models, we first examine the fits and residuals of two single AuNRs shown in Figures 2 and 3. The first AuNR (AuNR 1) shown in Figure 2 is approximately 113 nm × 38 nm (Figure 2A). The experimental emission image of this AuNR is shown in Figure 2B; this raw image is fit using each of the three models described above, and residuals

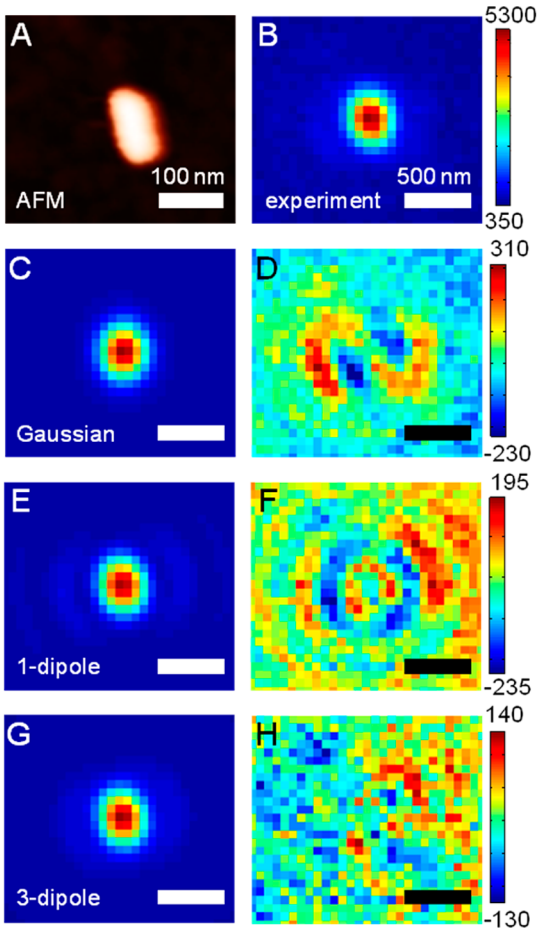

Figure 3. Comparison of different fits and corresponding residuals for AuNR 2. (A) AFM image of AuNR 2, with 25 nm maximum height. (B) Experimental AuNR 2 luminescence image. (C) Fit and (D) residuals of AuNR luminescence data using the 2-D Gaussian model. (E) Fit and (F) residuals using the 1-dipole PSF model. (G) Fit and (H) residuals using the 3-dipole PSF model with a single emission wavelength. Images B–H share a common 500 nm scale bar.

are calculated by subtracting the calculated PSF fit from the experimental data. The fit (Figure 2C) and residuals (Figure 2D) using the Gaussian model eq 1 show that the Gaussian PSF approximation is a nonideal fit for the AuNR luminescence image. Using the 1-dipole fit (Figure 2E), we see that the magnitude of the residuals decreases relative to the Gaussian model, but there are still strong systematic features in the residual image (Figure 2F). The 3-dipole model (single λ), shown in Figure 2G,H, produces residuals that are less than half the magnitude of the Gaussian residuals and are nearly randomly distributed across the field-of-view. Thus, the 3-dipole model (Figure 2G) is a better fit to the experimental data than the 1-dipole model (Figure 2E). This result is in agreement with previous studies, where fitting defocused images of AuNRs using a similar 3-dipole PSF algorithm yielded better fits than a 1-dipole model.[45,47] The same trend in residual patterns can be seen again in the second AuNR example (AuNR 2) shown in Figure 3, which shows fit and residual results for an AuNR of approximately 91 nm x 24 nm. Again we observe that the residuals are smaller and less regular as the model is changed from a 2-D Gaussian, to a 1-dipole PSF, and finally a 3-dipole PSF.

Selected fit results using several different PSFs on AuNR 1 are shown in Table 1. The 2-D Gaussian model provides the least amount of information about the AuNR 1 emission, yielding only the centroid position, but is 2 orders of magnitude faster than the next fastest fit. For convenience, the average x_0 and y_0 centroid values are arbitrarily set to zero for the 2-D Gaussian fit, and all other centroid positions are reported relative to these values for comparison of centroid localization accuracy. Next, we show the parameters associated with the 1-dipole model, in which we used the experimentally measured magnification of our optical microscope as a fixed parameter during the fit (denoted 1-dipole PSF (fixed mag.) in the table). This model fits values of φ, θ, and λ, in addition to the centroid position. The value of φ agrees very well with the orientation of the longitudinal dipole mode of the AuNR, based on the AFM image in the table. However, the model suggests that the AuNR is strongly tilted out-of-plane ($\theta = 74 \pm 1°$), whereas the associated AFM data indicated that the height of AuNR 1 only varied between 39.4 and 38.1 nm from end-to-end. We also find the centroid localization is extremely different between the 1-dipole and Gaussian models, with a difference of 7 nm in the x-position and 23 nm in the y-position. Lastly, we found that the 1-dipole model vastly overestimated the wavelength of the AuNR luminescence, as shown in Figure 4A. While the experimentally measured luminescence peak is at 660 nm, the 1-dipole model fits the emission at 721 $\pm$ 6 nm, which is much more red-shifted than expected.

To address this, we recalculated the 1-dipole fit, fixing the emission wavelength at the experimentally determined maximum value of 660 nm and fitting the magnification in addition to φ, θ, and the centroid position (denoted 1-dipole PSF (fixed λ) in the table). Because both emission wavelength and magnification affect the size of the imaged PSF, one of the two parameters needs to be fixed or the parameters can converge to incorrect values that are well outside the expected values. We see that the centroid location and three-dimensional AuNR orientation is unchanged between the two 1-dipole fits, but the magnification is now overestimated, as expected.

Next, we show the results from the 3-dipole model, in which only a single emission wavelength was fit in addition to φ, θ, and the centroid position (denoted 3-dipole PSF (single λ) in the table). While the value of φ is essentially unchanged between the 1-dipole and 3-dipole fits, we observe that θ increases to 85.8 $\pm$ 0.7° which is more consistent with the AFM data, although still slightly out-of-plane. We also find that the calculated emission wavelength of 665 $\pm$ 5 nm is in

TABLE 1. Parameter Values for Different Fitting Functions Applied to AuNR 1 from Figure 2[a]

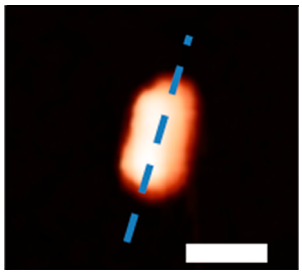

	φ (deg)	θ (deg)	λ (nm)	mag.	Δx (nm)	Δy (nm)	fit time[b]	R	K
2-D Gaussian	N.A.	N.A.	N.A.	N.A.	0(1)	0(2)	1 s	N.A	N.A.
1-dipole PSF (fixed mag.)	286.3(5)	74(1)	721(6)	262[c]	7(2)	−23(2)	6 min	1[c]	N.A.
1-dipole PSF (fixed λ)	286.3(5)	74(1)	660[c]	286(2)	7(1)	−23(2)	8 min	1[c]	N.A.
3-dipole PSF (single λ)	286.9(6)	85.8(7)	665(5)	262[c]	1(1)	−4(2)	18 min	0.72(5)	−0.1(3)
3-dipole PSF (multi-λ)[d]	287	85	672 (LM) 722 (TM) 693 (OOP)	262[c]	12	−4	80 min	0.8	0.4

[a] The dashed line on the AFM image indicates the fit φ value from the 3-dipole PSF (single-λ) fit (scale bar = 100 nm). Values in parentheses indicate the standard deviation (in the last significant digit) of the fit over 20 image frames. [b] Per frame, approximate. [c] Fixed parameter (experimentally measured). [d] Single frame fit.

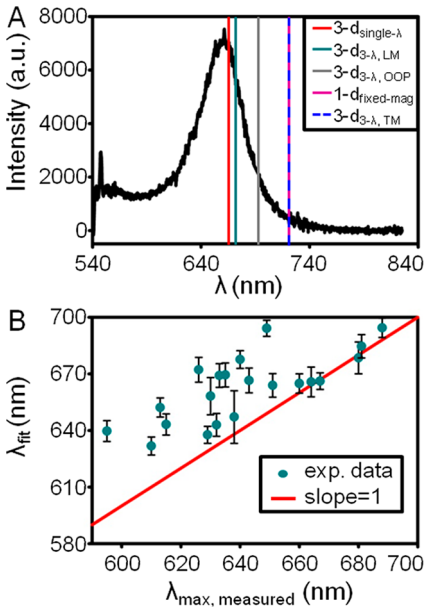

Figure 4. (A) Luminescence spectrum of AuNR 1 from Figure 2. Lines show the location of the calculated emission wavelengths for three different fits. For the 3-dipole fit where the emission wavelength of each dipole mode is fit independently, the corresponding wavelengths are indicated according to the mode assignment (LM, TM, and OOP). (B) Plot showing the relationship between the measured luminescence peak and the fitted emission wavelength using the 3-dipole PSF model of 21 AuNRs. A slope = 1 trendline is included for comparison.

excellent agreement with our experimental spectrum (Figure 4A). Based on the R value of 0.7, the emission is dominated by the longitudinal dipole mode, as expected, although there is a significant contribution from the transverse and out-of-plane modes as well. Lastly, we find that the difference between the Gaussian centroid position and 3-dipole centroid position are quite small compared to the 1-dipole model, with differences of 1 and 4 nm in the x- and y-directions, respectively.

In the final row of the table, we show the results of a 3-dipole model fit where the emission wavelengths for the three dipole components were allowed to vary (denoted 3-dipole PSF (multi-λ) in the table). This fit was tested because it is expected that if all of the emission is plasmon-mediated, then the transverse and out-of-plane modes would occur at shorter wavelengths than the longitudinal mode.[36,37] Based on the orientation of each axis of the 3-dipole fit, we assigned the three fit emission wavelengths to the LM, TM, and OOP components of the emission dipole (as shown in Figure 1B). Interestingly, all three dipole axis emission wavelengths fall to the red of both the measured luminescence peak and the 3-dipole single-λ fit (Figure 4A). The wavelengths determined for the TM and OOP dipole orientations are inconsistent with the expected blue-shifted wavelengths based on the results of references 36 and 37 (which show that nonlongitudinal mode polarized emission should be around the wavelength of the transverse plasmon mode of the AuNR). This suggests that the AuNR shows depolarized emission that is not mediated through the TM and OOP plasmon modes, consistent with results from Motegi *et al.*, where luminescence from AuNRs was often best fit to a 3-axis dipole, even when the wavelength of the transverse plasmon mode was well beneath the pass-band of their microscope dichroic.[45] This multiwavelength 3-dipole fit also yielded surprisingly poor localization accuracy, compared to the

TABLE 2. Parameter Values for Different Fitting Functions Applied to AuNR 2 from Figure 3[a]

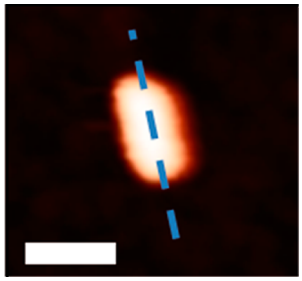

	φ (deg)	θ (deg)	λ (nm)	mag.	Δx (nm)	Δy (nm)	fit time[b]	R	K
2-D Gaussian	N.A.	N.A.	N.A.	N.A.	0(1)	0(2)	1 s	N.A	N.A.
1-dipole PSF (fixed mag.)	259.9(9)	89(2)	778(4)	262[c]	0(2)	0(3)	10 min	1[c]	N.A.
1-dipole PSF (fixed λ)	258.9(9)	90(2)	695[c]	293(1)	0(2)	0(2)	11 min	1[c]	N.A.
3-dipole PSF (single λ)	258.3(8)	89.8(2)	694(5)	262[c]	0(2)	0.1(9)	19 min	0.75(3)	−0.1(1)
3-dipole PSF (multi-λ)[d]	259	90	693 (LM) 635 (TM) 682 (OOP)	262[c]	−0.1	0.3	68 min	0.8	0.3

[a] The dashed line on the AFM image indicates the fit φ value from the 3-dipole PSF (single-λ) fit (scale bar =100 nm). Values in parentheses indicate the standard deviation (in the last significant digit) of the fit over 20 image frames. [b] Per frame, approximate. [c] Fixed parameter (experimentally measured). [d] Single frame fit.

single-wavelength 3-dipole fit, particularly in the x-dimension where a difference of 12 nm was calculated. Lastly, this fit was the most computationally expensive, requiring ~80 min to converge to a final result.

For comparison, Table 2 shows the same set of parameters for the different models for AuNR 2, which is found to be completely planar with respect to the surface ($\theta \approx 90°$ for all models in Table 2, fits and residuals shown in Figure 3). From the AFM data, the height of this nanorod was 23.2 and 23.6 nm, at each end, consistent with a planar structure. All models (except the 3-dipole multi-λ PSF) converge to the same average centroid location, indicating that localization accuracy is not improved by using a more complex dipole PSF model instead of a simple (and computationally inexpensive) Gaussian fit. We also find that all other trends described above are maintained in this second example. For example, we find that the value of φ for all models matches quite well with the orientation of the AuNR, as shown in the AFM image in the table. We also find that the 3-dipole single-λ PSF model fits to an emission wavelength of 694 $\pm$ 5 nm which is in excellent agreement with the experimental peak at 695 nm, while the 1-dipole fit is dramatically red-shifted to 778 $\pm$ 4 nm.

Since the 3-dipole (single λ) fit in the previous two examples provided the best overall agreement between the fitted wavelength and the peak in the experimental luminescence spectrum, we explored how well this model performed on other nanoparticles in our data set. In Figure 4B, we plot the emission wavelength fits for 21 individual AuNRs against their measured emission peak maximum. In this figure, we also include a line indicating where a relationship with a slope of one would lie in order to visualize the difference between the measured and fit values. We find that in all cases, the 3-dipole model produces an emission wavelength that either agrees with or is red-shifted relative to the actual AuNR emission with the average difference equal to 20 $\pm$ 20 nm. We also note that the wavelength fits tend to improve at longer wavelengths, where we observe much stronger agreement between our experimentally measured and fit wavelength values. We tested whether this improvement was related to the aspect ratio of the nanorod, but did not find an obvious correlation (Figures S7 and S8). For comparison, the average emission wavelength difference for the 1-dipole PSF fit is red-shifted by 69 nm $\pm$10 nm from the experimental peak.

Next, we compare the φ and θ estimates of the 1-dipole PSF (fixed mag) and 3-dipole (single λ) PSF models. Figure 5A−D, shows histograms of the φ and θ estimates with both PSF models for all 59 AuNRs examined for this study. The histograms for φ (Figure 5A,C) are distributed randomly from 0 to 360° as expected for an isotropic distribution of AuNRs on a surface. The θ values (Figure 5B,D), on the other hand, are clustered toward 90°, indicating that the AuNRs are lying mostly planar on the surface. However, we find that the 1-dipole fit (Figure 5B) tends to pull the θ values somewhat out of plane relative to the 3-dipole fit (Figure 5D). Figure 5E,F plots the φ and θ values, respectively, for the 1-dipole fit against the φ and θ values for the 3-dipole fit. In the case of φ (Figure 5E), both fits show excellent agreement, as evidenced by

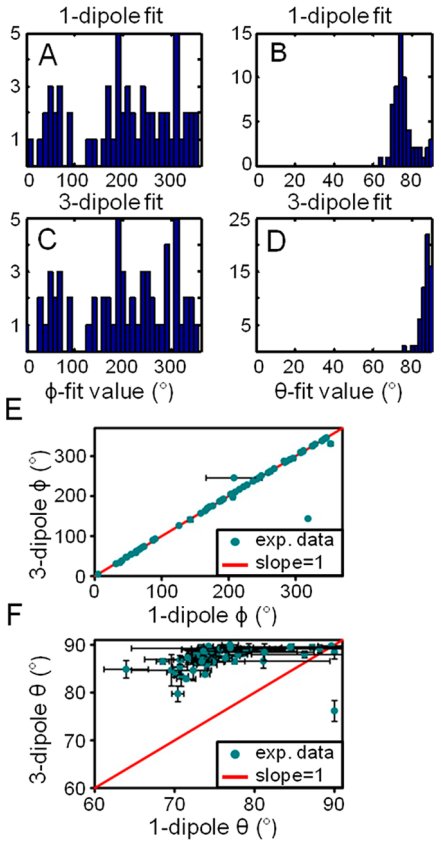

Figure 5. (A–D) Histograms showing fits to φ and θ for the 1-dipole and 3-dipole PSF super resolution fits for 59 different AuNR. (E and F) Plots showing the relationship of the φ values (E) and θ values (F) between the 1-dipole and 3-dipole PSF fits.

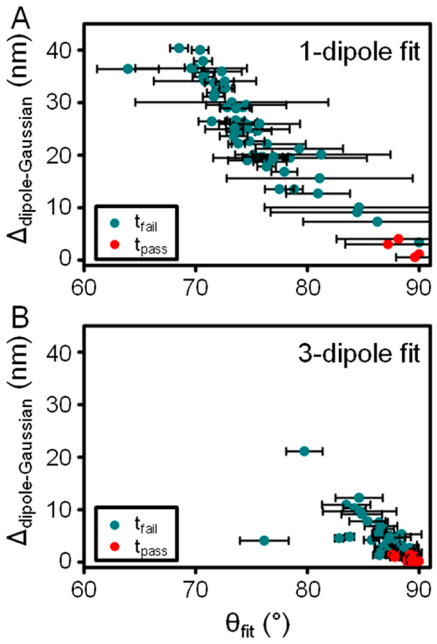

Figure 6. Plots showing the difference between the Gaussian centroid and the dipole PSF centroid (Δ) as a function of the fitted θ value. (A) 1-dipole PSF model. (B) 3-dipole PSF model. Colors indicate results of *t* testing dipole PSF fit centroids against a 2-D Gaussian fit (t_{fail} indicates statistically different centroid populations at α = 0.05, while t_{pass} indicates that the calculated centroids are the same within statistical error). Fits are shown for 59 individual AuNRs.

the bulk of the fits lying on the slope = 1 trendline (see Figure S1 for corresponding AFM images). On the other hand, the θ values show relatively poor agreement, with the 1-dipole fits often showing a larger out-of-plane orientation relative to the 3-dipole fits (Figure 5F). Additionally, the estimation of θ when using the 1-dipole PSF is of very low precision, as shown by the large error bars in Figure 5F.

Because of the symmetry of the AuNRs used in this study, a completely in-plane nanorod could fit to two possible values of φ (*e.g.*, φ_1 and φ_2) where $\varphi_1 = \varphi_2 + 180°$ (as in Figure 1). However, this symmetry is broken when the AuNR is out-of-plane, meaning that only one value of φ can accurately describe the data based on a given value of θ. For our fits, we chose an initial guess for φ_1 between 0 and 180° based on the orientation of the longitudinal axis of the AuNR as determined by AFM. We then fit the data a second time using φ_2 as the initial guess (our initial guess for θ was 90° for both fits). We found that for one initial guess of φ, the fitted value of θ would never move from 90°, while for the other initial guess of φ, the value of θ would fit to a slightly out-of-plane value (as in AuNR 1). Because the bounds for θ are defined between 0° and 90°, choosing the wrong initial guess for φ will not allow the fit to converge to the correct out-of-plane orientation, as the fit algorithm is unlikely to rotate the φ initial guess by 180° over the course of the fit. In 90% of cases where the fitted value of θ differed based on the initial guess for φ, we found that the average R^2 values of the fits over the 20 frames was better for the φ value that generated $\theta \neq 90°$. Thus, the initial guess of the in-plane orientation angle φ is critical for yielding the best overall fit when $\theta \neq 90°$ (note that this is not an issue in the Gaussian model, where no orientation parameters are included as initial guesses).

Given the large disagreement in θ between the 1-dipole and 3-dipole fits shown in Figure 5F, we next explored how the different dipole PSF models affected centroid localization accuracy relative to the 2-D Gaussian model. For this study, we calculated the distance (in nm) between the mean Gaussian centroid position (arbitrarily set to zero) and the mean position of a dipole PSF fit as $\Delta = \sqrt{\bar{x}_{PSF}^2 + \bar{y}_{PSF}^2}$. The result is plotted against the calculated θ values for 59 different AuNRs, as shown in Figure 6. In the case of the 1-dipole PSF fits (Figure 6A), the fit centroids show a large difference from the 2-D Gaussian fit centroids, with larger differences in Δ observed for smaller values of θ. We *t* tested these data (at $\alpha = 0.05$) and found that 55 of 59 (93%) of the total 1-dipole centroid positions were statistically different than the 2-D Gaussian centroid locations. Next, we plotted Δ against θ for the 3-dipole fit and found that the centroids from the 3-dipole fits

show much less deviation from the 2-D Gaussian centroid fits. In this case, 42 of 59 (71%) were statistically different at the 95% confidence level in the 3-dipole PSF fit. Thus, we find much better agreement between the simple, computationally inexpensive 2-D Gaussian and the more robust 3-dipole model, compared to the 1-dipole model. Importantly, this error in the centroid position is unrelated to the in-plane dipole angle, φ, given that we observe near identical φ values between the 1-dipole and 3-dipole fits (Figure 5E), and yet dramatically different localization accuracies.

Our data shows that utilizing a 3-dipole PSF to fit the experimental PSF of AuNR luminescence yields the best quality fit and therefore a more accurate determination of the emission centroid. Although we tried to test whether our calculated centroid positions agreed with the relative positions of individual nanorods in the AFM images, drift in the AFM prevented an accurate comparison; thus, our conclusion that the 3-dipole PSF fit is the best model is based purely on the agreement between experimental and theoretical results, both in the fitted values and in the associated residuals. By modeling the PSF incorrectly (*i.e.*, using a 1-dipole PSF in the case of AuNRs), the accuracy of the centroid determination can be even worse than when using a 2-D Gaussian model. This result should strongly inform the use of dipole PSF fitting in future studies, in that the PSF of the emission must be well understood before the proper model can be applied. In this study, we chose a strongly anisotropic nanostructure as a test system, which is expected to behave most like a single dipole relative to other nanostructures. Even with this system, we found that the 1-dipole model yielded poor localization accuracy, which was exacerbated by under-estimation of the inclination angle θ. We believe that this error is due to a small depolarized contribution to the luminescence, which is not radiated out through the higher-energy dipolar plasmon modes of the nanorod (*e.g.*, the TM or OOP modes). Given this depolarized emission, multiple dipoles were required to accurately model our experimental data, with emission fixed at a specific emission wavelength. Interestingly, Mortensen *et al.* have shown that when a diffraction-limited emitter is made up of many dipole emitters (such as a fluorophore-doped polystyrene sphere), a 2-D Gaussian will accurately describe the centroid location.[27] Our data also indicate that as more dipoles are included in the PSF model, a 2-D Gaussian shows higher overall agreement with the calculated centroid in comparison to the 1-dipole fit. This result has important implications for other plasmon-coupled emission processes, in which multiple dipole plasmon modes (possibly with different energies) may contribute to the measured emission PSF.[41−43] In these cases, a computationally inexpensive 2-D Gaussian may serve as a reasonable model of the emission PSF, particularly when any dominant dipolar emission modes are not oriented strongly out-of-plane. Lastly, we note that this study has focused largely on AuNRs that are oriented at fairly large values of θ relative to the substrate surface; this is due to the obvious asymmetry in the PSF which is introduced as emitters orient further out of plane (see Figure S9). In these cases, a 2-D Gaussian would clearly be a poor choice of fitting function for superlocalization studies, based on visual inspection alone. Thus, as always, care must be taken when choosing a fitting model for any super-resolution imaging experiment, whether emission is plasmon-mediated or not.

CONCLUSIONS

In this paper, we have applied a dipole emission PSF to the superlocalization fitting of luminescence from AuNRs. The 3-dipole PSF provided the best agreement between the fitted emission wavelength and the experimentally measured luminescence spectrum, and also yielded the lowest residuals compared to the 1-dipole PSF model and the 2-D Gaussian. This fit was also able to determine the dipole orientation parameters φ and θ with a precision below 1° in many cases, without the need for image defocusing, and the fitted φ-values were in good agreement with the orientation of the AuNR as determined *via* correlated AFM imaging. Thus, a 3-dipole PSF model increases localization accuracy over both a 2-D Gaussian fit and a 1-dipole fit for this system. We have also shown that AuNR localization accuracy using the 2-D Gaussian becomes worse as the dominant longitudinal dipole moves out-of-plane relative to the substrate surface, indicating the need for more robust fitting models. Additionally, care must be taken that the correct PSF model is used, as an incorrect dipole PSF model was shown to strongly skew the localization results *via* misestimation of the inclination angle θ. Thus, it is critical to consider multiple dipole contributions for localizing emission from complex emitters, especially in the case of plasmon-mediated emission processes.

METHODS

Sample Preparation. CTAB-stabilized gold nanorods were prepared using previously published methods.[54−56] One milliliter of a AuNR solution was centrifuged 3× at ~6700*g* for 20 min in order to remove excess surfactant, and a 2× concentrated solution of these AuNRs was used for experiments. Samples were prepared on alphanumerically patterned #1 glass coverslips for the purpose of AFM correlation. Slides were cleaned using Ar plasma for 10 min and then functionalized with APTES in a 0.5% solution in ethanol for an additional 10 min. To prepare samples, 5 μL of AuNR solution was dropcast onto the coverslip,

and allowed to sit for 5 min before being rinsed with nanopure water. This was followed by dropcasting 5 μL of a diluted sample of 200 or 500 nm diameter sky blue fluorescent polystyrene beads (Spherotech) in order to correct for mechanical drift. Samples were stored in the dark in a vacuum desiccator between preparation, optical experiments and AFM correlation.

Optical Experiments and Structural Correlation. Luminescence data was collected using an epi-illumination microscope configuration with a 1.3 NA, 100× oil-immersion objective lens. Diffraction-limited images were imaged onto an electron-multiplied CCD detector (ProEM, Princeton Instruments), and spectra were collected using a spectrometer with a liquid nitrogen cooled CCD detector (Acton 2500i/Princeton Instruments Spec-10). Excitation was *via* a 532 nm, circularly polarized laser at approximately 8.8 kW/cm^2, and emission was filtered using a dichroic/long-pass/notch filter combination with a cutoff of approximately 540 nm. Images of AuNR luminescence were collected using an integration time of 5 s.

AFM structural correlation was carried out by transferring the gridded sample to a combined optical/atomic force microscope after undertaking the optical studies.[38,39,57] Particles of interest were located using white-light total internal reflection excitation, and then imaged with the AFM (NT-MDT Integra-Vita) in semicontact mode. Sample orientation angles between the two microscopes were corrected *via* a triangulation method.

Image Processing. Before fitting, each image stack was corrected to remove background due to the fluorescence of the glass coverslip substrate. This was accomplished by fitting the average background of all frames in the stack to a 2-dimensional Gaussian, and then subtracting the fit from each image frame. The 2-dimensional Gaussian fits used for the super-resolution studies were written in-house using MATLAB, and are similar to what has been used in our previous studies.[13,17,18] The dipole PSF model was taken from Jörg Enderlein's "QDControl" program, which he has made available online.[49] The single- and 3-axis (single-λ) dipole PSFs were generated by fixing or releasing the parameters of κ and R in the "QDControl" PSF algorithm, while the 3-axis dipole PSF (multi-λ) was generated using 3 partially independent dipoles. Briefly, the calculated PSF consists of three independent single dipole PSFs which are summed to produce the final 3-dipole, multi-λ fit. The three dipoles are fixed in orientation and position relative to each other, such that the LM dipole mode is oriented at (φ, θ) and the other two (TM, OOP) are mutually orthogonal. The fit then proceeds as usual, but the emission wavelength and intensities of each dipole are allowed to vary, along with the combined centroid, total intensity, and orientational parameters that define the total PSF. Experimental images were fit to one of these PSF models using a bounded nonlinear least-squares fitting algorithm written in MATLAB.

Conflict of Interest: The authors declare no competing financial interest.

Supporting Information Available: AFM images of all AuNRs included in this study, information on the standard deviation of all fit estimates, histograms comparing planar and nonplanar AuNR centroid-localization, plots of wavelengths as a function of aspect ratio, PSF images for out-of-plane emitters, and details on microscope magnification determination. This material is available free of charge *via* the Internet at http://pubs.acs.org.

Acknowledgment. The authors thank Karole Blythe for synthesizing the AuNRs used in this study, as well as Prof. Jörg Enderlein for making his "QDControl" code available freely online. This material is based on work supported by the Welch Foundation under Award No. F-1699.

REFERENCES AND NOTES

1. Haes, A. J.; Haynes, C. L.; McFarland, A. D.; Schatz, G. C.; Van Duyne, R. P.; Zou, S. Plasmonic Materials for Surface-Enhanced Sensing and Spectroscopy. *MRS Bull.* **2005**, *30*, 368–375.
2. Willets, K. A.; Van Duyne, R. P. Localized Surface Plasmon Resonance Spectroscopy and Sensing. *Annu. Rev. Phys. Chem.* **2007**, *58*, 267–297.
3. Jain, P. K.; Huang, X.; El-Sayed, I. H.; El-Sayed, M. A. Noble Metals on the Nanoscale: Optical and Photothermal Properties and Some Applications in Imaging, Sensing, Biology, and Medicine. *Acc. Chem. Res.* **2008**, *41*, 1578–1586.
4. Lal, S.; Clare, S. E.; Halas, N. J. Nanoshell-Enabled Photothermal Cancer Therapy: Impending Clinical Impact. *Acc. Chem. Res.* **2008**, *41*, 1842–1851.
5. Stiles, P. L.; Dieringer, J. A.; Shah, N. C.; Van Duyne, R. P. Surface-Enhanced Raman Spectroscopy. *Annu. Rev. Anal. Chem.* **2008**, *1*, 601–626.
6. Golightly, R. S.; Doering, W. E.; Natan, M. J. Surface-Enhanced Raman Spectroscopy and Homeland Security: A Perfect Match? *ACS Nano* **2009**, *3*, 2859–2869.
7. Halas, N. J.; Lal, S.; Chang, W.-S.; Link, S.; Nordlander, P. Plasmons in Strongly Coupled Metallic Nanostructures. *Chem. Rev.* **2011**, *111*, 3913–3961.
8. Sagle, L. B.; Ruvuna, L. K.; Bingham, J. M.; Liu, C.; Cremer, P. S.; Van Duyne, R. P. Single Plasmonic Nanoparticle Tracking Studies of Solid Supported Bilayers with Ganglioside Lipids. *J. Am. Chem. Soc.* **2012**, *134*, 15832–15839.
9. Gu, Y.; Sun, W.; Wang, G.; Fang, N. Single Particle Orientation and Rotation Tracking Discloses Distinctive Rotational Dynamics of Drug Delivery Vectors on Live Cell Membranes. *J. Am. Chem. Soc.* **2011**, *133*, 5720–5723.
10. Gu, Y.; Wang, G.; Fang, N. Simultaneous Single-Particle Superlocalization and Rotational Tracking. *ACS Nano* **2013**, *7*, 1658–1665.
11. Gu, Y.; Di, X.; Sun, W.; Wang, G.; Fang, N. Three-Dimensional Super-Localization and Tracking of Single Gold Nanoparticles in Cells. *Anal. Chem.* **2012**, *84*, 4111–4117.
12. Marchuk, K.; Ha, J. W.; Fang, N. Three-Dimensional High-Resolution Rotational Tracking with Superlocalization Reveals Conformations of Surface-Bound Anisotropic Nanoparticles. *Nano Lett.* **2013**, *13*, 1245–1250.
13. Blythe, K. L.; Mayer, K. M.; Weber, M. L.; Willets, K. A. Ground State Depletion Microscopy for Imaging Interactions Between Gold Nanowires and Fluorophore-Labeled Ligands. *Phys. Chem. Chem. Phys.* **2013**, *15*, 4136–4145.
14. Lin, H.; Centeno, S. P.; Su, L.; Kenens, B.; Rocha, S.; Sliwa, M.; Hofkens, J.; Uji-i, H. Mapping of Surface-Enhanced Fluorescence on Metal Nanoparticles Using Super-Resolution Photoactivation Localization Microscopy. *ChemPhysChem* **2012**, *13*, 973–981.
15. Zhou, X.; Andoy, N. M.; Liu, G.; Choudhary, E.; Han, K.-S.; Shen, H.; Chen, P. Quantitative Super-resolution Imaging Uncovers Reactivity Patterns on Single Nanocatalysts. *Nat. Nanotechnol.* **2012**, *7*, 237–241.
16. Cang, H.; Labno, A.; Lu, C.; Yin, X.; Liu, M.; Gladden, C.; Liu, Y.; Zhang, X. Probing the Electromagnetic Field of a 15-Nanometre Hotspot by Single Molecule Imaging. *Nature* **2011**, *469*, 385–388.
17. Stranahan, S. M.; Willets, K. A. Super-Resolution Optical Imaging of Single-Molecule SERS Hot Spots. *Nano Lett.* **2010**, *10*, 3777–3784.
18. Weber, M. L.; Willets, K. A. Correlated Super-Resolution Optical and Structural Studies of Surface-Enhanced Raman Scattering Hot Spots in Silver Colloid Aggregates. *J. Phys. Chem. Lett.* **2011**, *2*, 1766–1770.
19. Weber, M. L.; Litz, J. P.; Masiello, D. J.; Willets, K. A. Super-Resolution Imaging Reveals a Difference Between SERS and Luminescence Centroids. *ACS Nano* **2012**, *6*, 1839–1848.
20. Titus, E. J.; Weber, M. L.; Stranahan, S. M.; Willets, K. A. Super-Resolution SERS Imaging beyond the Single-Molecule Limit: An Isotope-Edited Approach. *Nano Lett.* **2012**, *12*, 5103–5110.
21. Wei, L.; Liu, C.; Chen, B.; Zhou, P.; Li, H.; Xiao, L.; Yeung, E. S. Probing Single-Molecule Fluorescence Spectral Modulation Within Individual Hotspots with Subdiffraction-Limit Image Resolution. *Anal. Chem.* **2013**, *85*, 3789–3793.
22. Yildiz, A.; Forkey, J. N.; McKinney, S. A.; Ha, T.; Goldman, Y. E.; Selvin, P. R. Myosin V Walks Hand-Over-Hand: Single Fluorophore Imaging with 1.5-nm Localization. *Science* **2003**, *300*, 2061–2065.

23. Rust, M. J.; Bates, M.; Zhuang, X. Sub-Diffraction-Limit Imaging by Stochastic Optical Reconstruction Microscopy (STORM). *Nat. Methods* **2006**, *3*, 793–796.
24. Betzig, E.; Patterson, G. H.; Sougrat, R.; Lindwasser, O. W.; Olenych, S.; Bonifacino, J. S.; Davidson, M. W.; Lippincott-Schwartz, J.; Hess, H. F. Imaging Intracellular Fluorescent Proteins at Nanometer Resolution. *Science* **2006**, *313*, 1642–1645.
25. Enderlein, J.; Toprak, E.; Selvin, P. R. Polarization Effect on Position Accuracy of Fluorophore Localization. *Opt. Express* **2006**, *14*, 8111–8120.
26. Lew, M. D.; Backlund, M. P.; Moerner, W. E. Rotational Mobility of Single Molecules Affects Localization Accuracy in Super-Resolution Fluorescence Microscopy. *Nano Lett.* **2013**, 10.1021/nl304359p.
27. Mortensen, K. I.; Churchman, L. S.; Spudich, J. A.; Flyvbjerg, H. Optimized Localization Analysis for Single-Molecule Tracking and Super-Resolution Microscopy. *Nat. Methods* **2010**, *7*, 377–381.
28. Engelhardt, J.; Keller, J.; Hoyer, P.; Reuss, M.; Staudt, T.; Hell, S. W. Molecular Orientation Affects Localization Accuracy in Superresolution Far-Field Fluorescence Microscopy. *Nano Lett.* **2011**, *11*, 209–213.
29. Bartko, A. P.; Dickson, R. M. Three-Dimensional Orientations of Polymer-Bound Single Molecules. *J. Phys. Chem. B* **1999**, *103*, 3053–3056.
30. Bartko, A. P.; Dickson, R. M. Imaging Three-Dimensional Single Molecule Orientations. *J. Phys. Chem. B* **1999**, *103*, 11237–11241.
31. Hellen, E. H.; Axelrod, D. Fluorescence Emission at Dielectric and Metal-Film Interfaces. *J. Opt. Soc. Am. B* **1987**, *4*, 337–350.
32. Dickson, R. M.; Norris, D. J.; Moerner, W. E. Simultaneous Imaging of Individual Molecules Aligned Both Parallel and Perpendicular to the Optic Axis. *Phys. Rev. Lett.* **1998**, *81*, 5322–5325.
33. Böhmer, M.; Enderlein, J. Orientation Imaging of Single Molecules by Wide-Field Epifluorescence Microscopy. *J. Opt. Soc. Am. B* **2003**, *20*, 554–559.
34. Lieb, M. A.; Zavislan, J. M.; Novotny, L. Single-Molecule Orientations Determined by Direct Emission Pattern Imaging. *J. Opt. Soc. Am. B* **2004**, *21*, 1210–1215.
35. Fang, Y.; Chang, W.-S.; Willingham, B.; Swanglap, P.; Dominguez-Medina, S.; Link, S. Plasmon Emission Quantum Yield of Single Gold Nanorods as a Function of Aspect Ratio. *ACS Nano* **2012**, *6*, 7177–7184.
36. Tcherniak, A.; Dominguez-Medina, S.; Chang, W.-S.; Swanglap, P.; Slaughter, L. S.; Landes, C. F.; Link, S. One-Photon Plasmon Luminescence and Its Application to Correlation Spectroscopy as a Probe for Rotational and Translational Dynamics of Gold Nanorods. *J. Phys. Chem. C* **2011**, *115*, 15938–15949.
37. Yorulmaz, M.; Khatua, S.; Zijlstra, P.; Gaiduk, A.; Orrit, M. Luminescence Quantum Yield of Single Gold Nanorods. *Nano Lett.* **2012**, *12*, 4385–4391.
38. Stranahan, S. M.; Titus, E. J.; Willets, K. A. SERS Orientational Imaging of Silver Nanoparticle Dimers. *J. Phys. Chem. Lett.* **2011**, *2*, 2711–2715.
39. Stranahan, S. M.; Titus, E. J.; Willets, K. A. Discriminating Nanoparticle Dimers from Higher Order Aggregates through Wavelength-Dependent SERS Orientational Imaging. *ACS Nano* **2012**, *6*, 1806–1813.
40. Ausman, L. K.; Schatz, G. C. On the Importance of Incorporating Dipole Reradiation in the Modeling of Surface Enhanced Raman Scattering from Spheres. *J. Chem. Phys.* **2009**, *131*, 084708–084708−10.
41. Li, Z.; Shegai, T.; Haran, G.; Xu, H. Multiple-Particle Nanoantennas for Enormous Enhancement and Polarization Control of Light Emission. *ACS Nano* **2009**, *3*, 637–642.
42. Shegai, T.; Li, Z.; Dadosh, T.; Zhang, Z.; Xu, H.; Haran, G. Managing Light Polarization *via* Plasmon−Molecule Interactions Within an Asymmetric Metal Nanoparticle Trimer. *Proc. Natl. Acad. Sci. U.S.A.* **2008**, *105*, 16448–16453.
43. Shegai, T.; Brian, B.; Miljković, V. D.; Käll, M. Angular Distribution of Surface-Enhanced Raman Scattering from Individual Au Nanoparticle Aggregates. *ACS Nano* **2011**, *5*, 2036–2041.
44. Xiao, L.; Qiao, Y.; He, Y.; Yeung, E. S. Three Dimensional Orientational Imaging of Nanoparticles with Darkfield Microscopy. *Anal. Chem.* **2010**, *82*, 5268–5274.
45. Motegi, T.; Nabika, H.; Niidome, Y.; Murakoshi, K. Observation of Defocus Images of a Single Metal Nanorod. *J. Phys. Chem. C* **2013**, *117*, 2535–2540.
46. Ha, J. W.; Marchuk, K.; Fang, N. Focused Orientation and Position Imaging (FOPI) of Single Anisotropic Plasmonic Nanoparticles by Total Internal Reflection Scattering Microscopy. *Nano Lett.* **2012**, *12*, 4282–4288.
47. Li, T.; Li, Q.; Xu, Y.; Chen, X.-J.; Dai, Q.-F.; Liu, H.; Lan, S.; Tie, S.; Wu, L.-J. Three-Dimensional Orientation Sensors by Defocused Imaging of Gold Nanorods through an Ordinary Wide-Field Microscope. *ACS Nano* **2012**, *6*, 1268–1277.
48. Wackenhut, F.; Virgilio Failla, A.; Züchner, T.; Steiner, M.; Meixner, A. J. Three-Dimensional Photoluminescence Mapping and Emission Anisotropy of Single Gold Nanorods. *Appl. Phys. Lett.* **2012**, *100*, 263102–263102−4.
49. Enderlein, J. Imaging of Single Molecules. http://www.joerg-enderlein.de/imagingOfSingleMolecules.html (accessed May 3, 2013).
50. Patra, D.; Gregor, I.; Enderlein, J. Image Analysis of Defocused Single-Molecule Images for Three-Dimensional Molecule Orientation Studies. *J. Phys. Chem. A* **2004**, *108*, 6836–6841.
51. Patra, D.; Gregor, I.; Enderlein, J.; Sauer, M. Defocused Imaging of Quantum-Dot Angular Distribution of Radiation. *Appl. Phys. Lett.* **2005**, *87*, 101103–101103−3.
52. Dulkeith, E.; Niedereichholz, T.; Klar, T. A.; Feldmann, J.; von Plessen, G.; Gittins, D. I.; Mayya, K. S.; Caruso, F. Plasmon Emission in Photoexcited Gold Nanoparticles. *Phys. Rev. B* **2004**, *70*, 205424.
53. Varnavski, O. P.; Goodson, T.; Mohamed, M. B.; El-Sayed, M. A. Femtosecond Excitation Dynamics in Gold Nanospheres and Nanorods. *Phys. Rev. B* **2005**, *72*, 235405.
54. Ming, T.; Zhao, L.; Yang, Z.; Chen, H.; Sun, L.; Wang, J.; Yan, C. Strong Polarization Dependence of Plasmon-Enhanced Fluorescence on Single Gold Nanorods. *Nano Lett.* **2009**, *9*, 3896–3903.
55. Liao, H.; Hafner, J. H. Gold Nanorod Bioconjugates. *Chem. Mater.* **2005**, *17*, 4636–4641.
56. Mayer, K. M.; Lee, S.; Liao, H.; Rostro, B. C.; Fuentes, A.; Scully, P. T.; Nehl, C. L.; Hafner, J. H. A Label-Free Immunoassay Based Upon Localized Surface Plasmon Resonance of Gold Nanorods. *ACS Nano* **2008**, *2*, 687–692.
57. Kaplan-Ashiri, I.; Titus, E. J.; Willets, K. A. Subdiffraction-Limited Far-Field Raman Spectroscopy of Single Carbon Nanotubes: An Unenhanced Approach. *ACS Nano* **2011**, *5*, 1033–1041.